toxics

MDPI

Article

Aging Process of Sea Salt Particles Driven by Glyoxal: Implications for Climate Effects

Yongpeng Ji [1,2], Zhiming Zhang [1,2], Shengping Chen [1,2], Qiuju Shi [1,2], Jiaxin Wang [1,2], Baocong Zhao [1,2], Weina Zhang [1,2], Jiangyao Chen [1,2] and Yuemeng Ji [1,2,*]

[1] Guangdong-Hong Kong-Macao Joint Laboratory for Contaminants Exposure and Health, Guangdong Key Laboratory of Environmental Catalysis and Health Risk Control, Institute Environmental Health and Pollution Control, Guangdong University of Technology, Guangzhou 510006, China
[2] Guangdong Basic Research Center of Excellence for Ecological Security and Green Development, Key Laboratory of City Cluster Environmental Safety and Green Development of the Ministry of Education, School of Environmental Science and Engineering, Guangdong University of Technology, Guangzhou 510006, China
* Correspondence: jiym@gdut.edu.cn

Abstract

Atmospheric sea spray aerosol (SSA) undergoes chemical aging during long-distance transport, leading to significant alterations in its climate effects. However, the aging mechanisms of SSA driven by oxygenated volatile organic compounds (OVOCs) remain unclear. Hence, the aging processes of NaCl particles driven by glyoxal (GL), a representative OVOC, are systematically investigated using molecular dynamics (MD) simulations and density functional theory (DFT) calculations. MD simulations with high GL coverage show that GL readily mixes with NaCl and preferentially orients its carbonyl groups toward the NaCl surface. The adsorption of GL on the NaCl surface is dominated by the interaction between the O atom of GL (O_{GL}) and the Na atom of the surface. DFT calculations with single GL coverage further reveal the formation of the O_{GL}–Na bond between GL and NaCl. The mixing process of GL and NaCl is regulated by both the number of aldehyde groups engaging in the interfacial coordination and the corresponding lengths of O_{GL}–Na bonds. The subsequent heterogeneous oxidation of GL by an OH radical proceeds mainly via a barrierless H-abstraction pathway to form HC(O)CO radicals, which may further react with methylamine/ammonia and contribute to brown carbon formation. Our results reveal the importance of incorporating such aging mechanisms into atmospheric models to improve climate predictions.

Keywords: heterogeneous oxidation; reaction mechanisms; glyoxal; theoretical calculations; mixing processes

Academic Editor: Matthias Karl

Received: 1 April 2026
Revised: 7 May 2026
Accepted: 8 May 2026
Published: 10 May 2026

1. Introduction

Atmospheric sea spray aerosol (SSA) is one of the most abundant natural aerosol sources and plays a fundamental role in the global cycling of key elements, including sulfur, nitrogen, and halogens [1]. SSA, which is primarily generated through wind-driven wave breaking and bubble bursting at the ocean surface [2], is emitted into the atmosphere from oceans with an estimated global flux of 16,600 Tg y^{-1} [3]. The emitted SSA is dominated by inorganic salts, particularly sodium chloride (NaCl), and typically exhibits a core–shell structure with a crystalline NaCl core [4]. SSA significantly influences Earth's radiation budget and global climate by directly scattering and absorbing solar radiation and indirectly acting as cloud condensation nuclei (CCN) or ice nuclei (IN) [2,5–7]. Once

emitted, SSA particles can undergo long-distance transport, reaching inland regions [8]. During this process, SSA serves as an important reactive interface for heterogeneous chemical processes of atmospheric species [4]. Moreover, the mixing of atmospheric species with SSA, along with subsequent interfacial reactions on SSA, drives the chemical aging of SSA. This process modifies the chemical composition, morphology, and mixing state of SSA, resulting in pronounced changes in CCN activity and optical properties [4,9–12]. Hence, the environmental and climatic effects of SSA are significantly dependent on its atmospheric aging.

Previous studies [4,10,11,13–18] have demonstrated that SSA can mix with a wide range of atmospheric components during long-distance transport, including inorganic and organic compounds, dusts, heavy metals, and volcanic aerosols, resulting in alterations of its physiochemical properties. For example, a field observation shows that the mixing of sea salt particles with mineral dust during dust periods results in a reduction in their hygroscopicity [10]. In addition, deliquescence-mode experiments with mixed aerosol particles of NaCl and $MgSO_4$ reveal that the Mg salts ($MgSO_4$ and the formed $MgCl_2$) that are enriched at the particle surface can lower the deliquescence point of NaCl particles [17]. Notably, organic species play a significant role in the aging of SSA. A modeling study has reported that hygroscopic growth of SSA is suppressed by 4–20% via the internal mixing with organic compounds under high relative humidity, and light scattering is also reduced by up to 37%, leading to an attenuation of the radiative cooling effect of SSA [11]. In addition, an experimental study by Ghorai et al. has revealed that when mixed with malonic acid and glutaric acid, cubic crystalline NaCl is modified into rounded particles, and its hygroscopic growth is suppressed [15]. Hence, the mixing of organic compounds with SSA, along with their subsequent heterogeneous reactions, plays a critical role in determining the physicochemical properties of SSA.

Oxygenated volatile organic compounds (OVOCs), which represent an important class of organic species due to their high abundance and reactivity, are primarily emitted from vehicular exhaust and secondary atmospheric chemical processes [19]. In addition, they can be introduced into the atmosphere through emissions from biological sources [20], hydrocarbon oxidation [21], the evaporation of oxygenated solvents or fuels, as well as incomplete combustion from mobile and stationary hydrocarbon-fueled sources [22]. Previous studies have shown that the photooxidation of OVOCs plays an important role in the formation of secondary organic aerosols (SOA) and tropospheric ozone (O_3) [23–27]. Glyoxal (GL) is one of the most abundant and reactive OVOCs in the atmosphere. Owing to its high reactivity and water solubility, GL can easily enter the particle phase and plays a crucial role in the formation of SOA [28–31]. Except for the reaction in the gas phase [32,33] and aqueous phase [34–38], the heterogeneous reaction of GL on atmospheric particles [39–44] is an important sink of GL. Some studies have shown that the mixing of GL with mineral particles has formed oligomers, organosulfates and organic acid on mineral particles, which altered the optical properties, particle size and hygroscopicity of mineral particles [39,45]. However, the aging mechanism of SSA driven by GL remains unclear.

Hence, we performed a theoretical approach to investigate the GL-driven aging processes of a NaCl particle, the dominant component of SSA. Using molecular dynamics (MD) simulations, the mixing behavior of NaCl particles with GL was elucidated. GL-driven adsorption modes on the NaCl particles were characterized by density functional theory (DFT) calculations. Charge density difference (CDD) analysis was performed to reveal the nature of the interfacial interaction between GL and NaCl and the mixing mechanisms. In addition, the heterogeneous oxidation mechanisms of GL by OH radicals were further established and the implications of the GL-driven aging processes of NaCl on the atmosphere were discussed.

2. Computational Methods

2.1. Molecular Dynamics Simulations

All classical MD simulations were performed using the large-scale atomic/molecular massively parallel simulator (LAMMPS) package [46]. Since NaCl constitutes the dominant component (approximately 90%) of fresh SSA [1] and is widely used as a representative of SSA [47,48], NaCl (001) was selected as a simplified model of SSA in this work. A (18 × 18) NaCl (001) slab model (denoted as NaCl hereinafter) with 10 atomic layers was constructed for MD simulations. The NaCl (001) slab was centered in the simulation box with dimensions of 97 × 97 × 122 Å^3 in x, y, and z directions, respectively. A total of 25 gaseous GL molecules were inserted into the vacuum region of the simulation box to construct the mixing system of NaCl (001) and GL according to the ideal gas equation (Equation (1)):

$$pV = nRT \quad (1)$$

where p, V, n, R and T represent pressure, volume, number of gaseous molecules, the universal gas constant and temperature, respectively. A 5.0 ns MD simulation with the time step of 1.0 fs was carried out in the isothermal–isobaric (*NPT*) ensemble (P = 1 atm, T = 298.15 K) using the Nosé–Hoover thermostat and barostat, respectively, to guarantee the thermodynamic equilibrium of each mixing system [49,50]. NaCl was described from Joung and Cheatham parameters [51], while GL was described by the General Amber Force Field (GAFF) force field [52] with the restrained electrostatic potential (RESP) charge. The periodic boundary conditions were applied in all three dimensions. A cut-off distance of 12.0 Å was used for the short-range interactions. The long-range electrostatic interactions were computed using the particle–particle–particle–mesh (PPPM) summation algorithm with a dimensionless accuracy of 1×10^{-5} [53]. The analyses of the atomic density profiles were calculated according to Equation (2):

$$\rho(z) = \frac{N(\Delta z)}{V} \quad (2)$$

where $\rho(z)$ is the density in the z direction, $N(\Delta z)$ is the average number of atoms in a small bin of thickness Δz in the z-axis of the simulation box and V denotes the volume of the simulation box.

2.2. Density Function Theory Calculations

All DFT calculations were performed using the Vienna ab initio simulation package (VASP, version 5.4.4) [54]. A (3 × 3) NaCl (001) surface with a four-layer slab was constructed to simulate the sea salt surface. For all calculations, the Perdew–Burke–Ernzerhof (PBE) [55] generalized gradient approximation (GGA) exchange–correlation functional was used to treat the electron interactions. The core electrons were described with the projector augmented wave (PAW) method [56]. The plane-wave kinetic energy cutoff was set to 400 eV, and the convergence criterion of structural optimization was −0.01 eV/Å. The vacuum region was set to approximately 30 Å to eliminate the interlayer interactions. A 2 × 2 × 1 Monkhorst–Pack k-point grid was applied. The dispersion corrections were considered using the DFT-D3(BJ) scheme [57,58]. The climbing nudged elastic band method [59] and the improve dimer methods [60] were performed to confirm the transition states (TSs) with the convergence criterion of −0.05 eV/Å. In this work, the adsorption energy (ΔE) is defined as $\Delta E = E_{(\text{NaCl-GL})} - (E_{\text{NaCl}} + E_{\text{GL}})$, where $E_{(\text{NaCl-GL})}$ represents the total energy of the mixing system and E_{NaCl} and E_{GL} are the energies of NaCl and GL, respectively. The energy barrier is defined as $E_{\text{TS}} - E_{\text{IS}}$, and reaction energy is defined as $E_{\text{FS}} - E_{\text{IS}}$, where E_{TS}, E_{IS} and E_{FS} represent the energies of the TSs, initial states (ISs),

and final states (FSs) in the corresponding pathways, respectively. CDD was calculated to investigate the charge transfer between GL and the NaCl surface, which is defined as the difference between the charge densities of the mixing system of GL-NaCl and the sum of the charge densities of the isolated GL and the NaCl surface. CDD results were visualized using the VESTA package [61]. Considering the compositional complexity of real SSA, other inorganic ions were not explicitly included in the present model, which may introduce certain limitations. However, this simplified model provides a fundamental basis for understanding the mixing of GL and SSA at the molecular level.

3. Results and Discussion

3.1. Mixing Processes of GL with NaCl

The mixing process of GL with NaCl, which represents the initial step of the GL-driven aging of NaCl, was simulated using MD simulations. Several representative snapshots of the mixing process of GL with NaCl shown in Figure S1 reveal that GL readily adsorbs onto the NaCl surface and exhibits distinct orientations, leading to the formation of different adsorption configurations. To systematically characterize these adsorption configurations, the orientation of GL relative to the surface was quantified by using the cos(θ) value, where θ is defined as the angle between the *z*-axis (perpendicular to the surface) and the carbonyl group of GL. A value of 0 corresponds to the carbonyl group being completely parallel to the NaCl surface, while a value of 1 indicates a perpendicular orientation with the carbonyl group pointing toward the surface. The probability distributions of cos(θ) are shown in Figure 1a. A broad maximum centered around 0.8 and a noticeable population at 0 are observed, corresponding to configurations in which the carbonyl group points to the surface and lies parallel to the surface, respectively. The relatively broad distribution around 0.8 suggests that the carbonyl group is predominantly oriented toward the NaCl surface, implying that it may serve as the active site of GL to interact with NaCl.

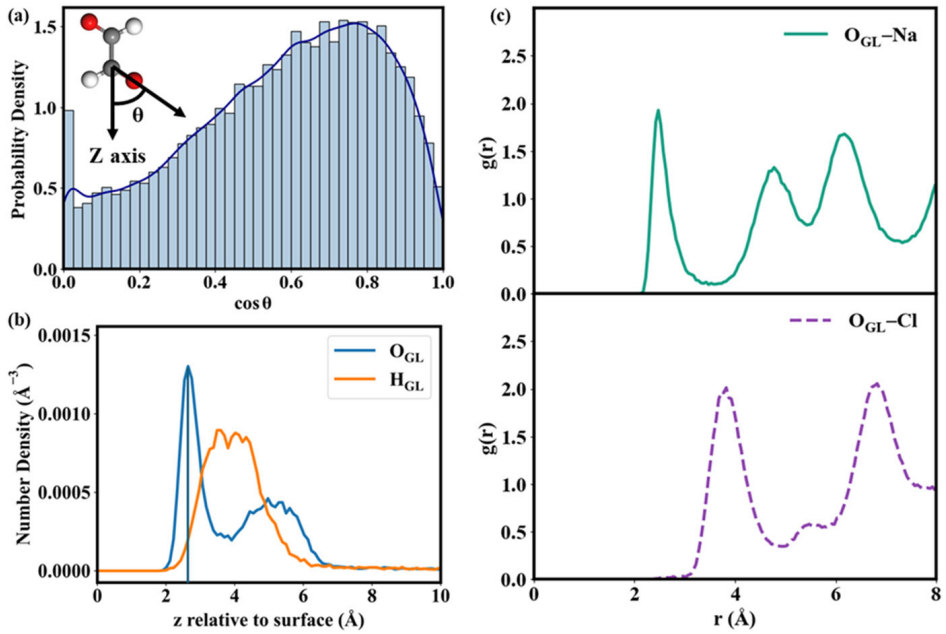

Figure 1. (**a**) Molecular orientation distributions of GL molecules on NaCl surfaces. (**b**) Atomic density profiles (ADPs) of GL as a function of distance from NaCl surfaces. *z* = 0 Å are the mean positions for the Na atoms of the NaCl surface. The locations of the ADP peaks represent the average distance between the corresponding atoms and NaCl surfaces. (**c**) Radial distribution functions (RDFs) for the possible atomic pairs between O_{GL} and NaCl surface.

To clarify the main active site of GL interacting with the NaCl surface, atomic density profiles (ADPs) of GL were calculated as functions of the distance normal to the NaCl surface and are shown in Figure 1b. Analysis of ADPs indicates that the interaction between GL and the NaCl surface is predominantly driven by the O atoms of GL (O_{GL}), as evidenced by the positions of the ADP peak centers for O_{GL} and H_{GL} at ~2.5 Å and ~4.0 Å, respectively. The shorter distance of the O_{GL} to the surface suggests that O_{GL} serves as the primary interaction site of GL to interact with NaCl. Hence, the possible atomic pairs involved in the interaction between O_{GL} and the NaCl surface, i.e., O_{GL}–Na and O_{GL}–Cl, are further examined by radial distribution functions (RDFs), which quantify the probability of finding a given atom at a distance *r* from a reference atom. As delineated in Figure 1c, the RDF for O_{GL}–Na exhibits a pronounced first peak at approximately 2.5 Å, while the first peak of O_{GL}–Cl occurs at a longer distance of approximately 4.2 Å, with a comparable RDF intensity to that of O_{GL}–Na. It indicates a stronger interaction between O_{GL} and Na atoms relative to that between O_{GL} and Cl atoms. Hence, GL can be effectively adsorbed on the NaCl surface, which is predominantly driven by the interaction between O_{GL} and Na atoms.

3.2. Mixing Mechanisms of GL with NaCl

To understand the mixing mechanisms of GL with NaCl at the atomic level, adsorption configurations of GL on the NaCl surface were identified using DFT calculations. The optimized geometries of all adsorption configurations are presented in Figures 2 and S2, while the potential energy surfaces of all possible mixing pathways are shown in Figures 3 and S3. Depending on the number of O_{GL}–Na bonds formed in adsorption configurations, three types of interaction modes were identified: Type A, where GL is adsorbed on NaCl with the formation of one O_{GL}–Na bond; Type B, where GL is adsorbed on NaCl with the formation of two O_{GL}–Na bonds; and Type C, where GL is adsorbed on NaCl without forming an O_{GL}–Na bond. For Type A, five adsorption configurations were identified. Except for the O_{GL}–Na bond, there exists an extra H_{GL}–Cl bond between GL and NaCl in GL-NaCl-A1/2, with the bond length of 2.68 Å (Figure 2). The lengths of the O_{GL}–Na bonds in GL-NaCl-A1 and GL-NaCl-A2 are 2.43 and 2.40 Å, respectively, suggesting a slightly stronger interaction between the O_{GL} and Na atoms in GL-NaCl-A2. However, the ΔE of GL-NaCl-A2 with -8.95 kcal mol^{-1} is 1.60 kcal mol^{-1} higher than that of GL-NaCl-A1 (Figure 3), indicating a stronger interaction between GL and NaCl in GL-NaCl-A1 than that in GL-NaCl-A2. This is attributed to the number of aldehyde groups of GL involved in the interaction. As shown in Figure 2, GL interacts with NaCl via both aldehyde groups in GL-NaCl-A1, while a single aldehyde group of GL participates in the interaction in GL-NaCl-A2. Similar results can also be drawn in three other adsorption configurations (Figure S2). The ΔE of GL-NaCl-A5, where GL interacts with NaCl via a single aldehyde group, is calculated to be -8.86 kcal mol^{-1}, which is at least 1.64 kcal mol^{-1} higher than those of GL-NaCl-A3 and GL-NaCl-A4 (Figure S3).

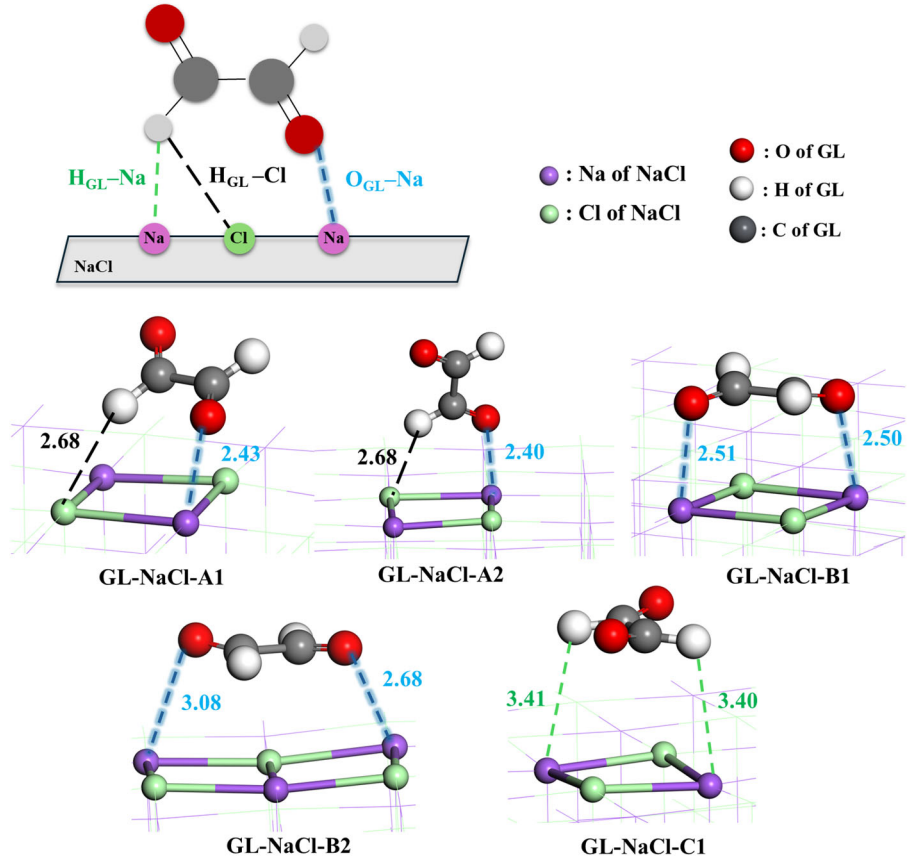

Figure 2. Optimized geometries for adsorption configurations of GL on the NaCl surface along with the scheme of bonds formed between GL and NaCl in adsorption configurations (bond length in Å).

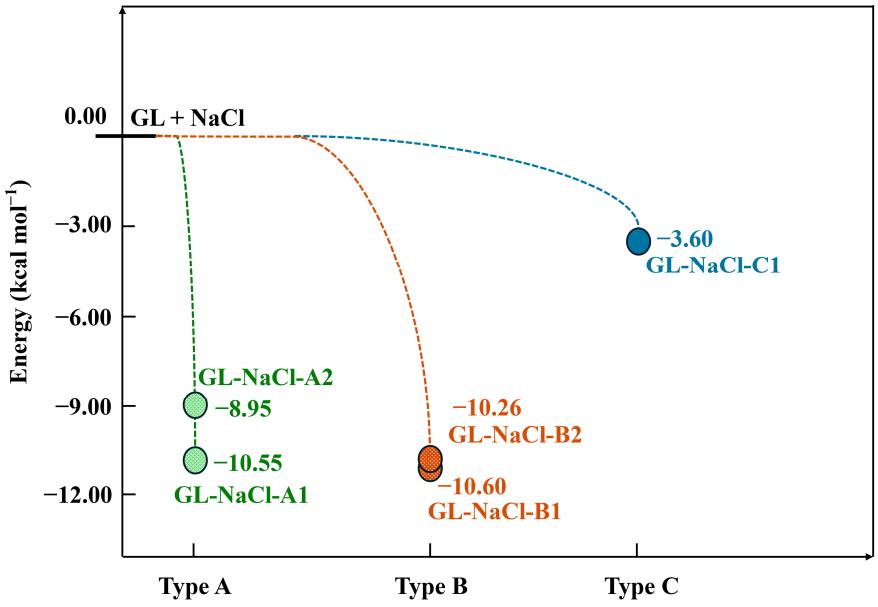

Figure 3. Potential energy surfaces for mixing pathways of GL with NaCl.

For Type B, two adsorption configurations were identified. In GL-NaCl-B1, two O_{GL}–Na bonds with bond lengths of 2.50 and 2.51 Å are formed, which are both shorter than those in GL-NaCl-B2 (Figure 2), indicating a stronger interaction between GL and NaCl in GL-NaCl-B1. The ΔE of GL-NaCl-B1 (−10.60 kcal mol^{-1}) is 0.34 kcal mol^{-1} lower than that of GL-NaCl-B2 (Figure 3), further supporting the correlation between shorter O_{GL}–Na bond lengths and stronger interaction strength. Compared the dominant configuration between

Type A and Type B, the ΔE of GL-NaCl-B1 is only 0.05 kcal mol^{-1} lower than that of GL-NaCl-A1 (Figure 3). The difference in ΔE is smaller than the thermal energy at ambient temperature, indicating that the contributions of Type A and Type B configurations to the mixing of GL and NaCl should not be evaluated solely based on adsorption energies. As revealed by the broad cos(θ) distribution in the MD simulations (Figure 1a), GL molecules exhibit a wide range of interfacial orientations. Type B configurations require the simultaneous formation of two O_{GL}–Na bonds and thus impose stronger orientational constraints, while Type A configurations retain greater rotational and configurational freedom. This indicates that although GL-NaCl-A1 has a higher adsorption energy than GL-NaCl-B1, Type A configurations remain competitive.

For Type C, only one adsorption configuration is identified. As shown in GL-NaCl-C1 (Figure 2), no O_{GL}–Na bond is formed between GL and NaCl, but two O_{GL}–Cl bonds are formed, with the bond lengths of 3.40 and 3.41 Å. The corresponding ΔE of GL-NaCl-C1 is at least 5.35 kcal mol^{-1} higher than those of the adsorption configurations in Type A and B, indicating that this interaction mode is of minor importance for the mixing of GL and NaCl (Figure 3). This result is consistent with MD simulations, which show that the interaction between O_{GL} and Na dominates the mixing of GL and NaCl.

To further elucidate the nature of the interaction between GL and NaCl, CDD analysis of the above configurations was performed, and the results are shown in Figure 4. Except for GL-NaCl-C1, all configurations clearly exhibit the pronounced electron accumulation around the O_{GL} and the corresponding electron depletion around the surface Na atom, indicating significant charge transfer from the Na atom to the O_{GL} atom. However, GL-NaCl-C1, without the formation of an O_{GL}–Na bond, shows a weak charge transfer. It is consistent with the weaker interaction between GL and NaCl, confirming that such interactions play a minor role in the mixing process. For Type A, GL-NaCl-A1, in which both aldehyde groups participate in the interactions, exhibits more extensive charge transfer than GL-NaCl-A2, where only one aldehyde group is involved. It suggests that the number of aldehyde groups participating in the interaction plays a dominant role in regulating the mixing process. Similarly, for Type B, the charge transfer between O_{GL} and the Na atom in GL-NaCl-B1 is stronger than that in GL-NaCl-B2, in line with the shorter O_{GL}–Na bonds. Hence, the mixing of GL and NaCl is regulated by the number of aldehyde groups that participate in the interaction and the bond lengths of O_{GL}–Na.

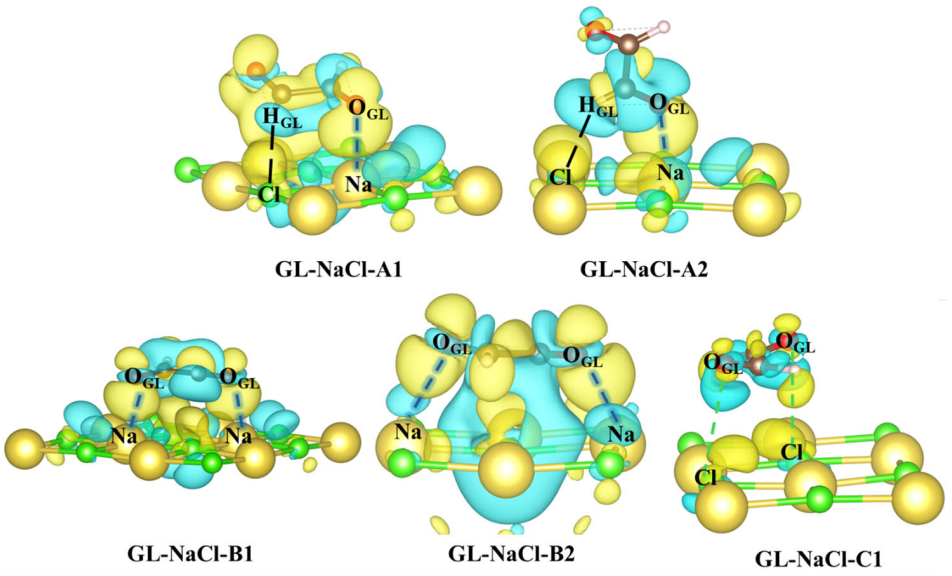

Figure 4. Charge density difference for adsorption configurations of GL on the NaCl surface, where the yellow and blue parts represent the area gaining and losing electrons, respectively.

3.3. Heterogeneous Oxidation Mechanisms of GL on NaCl Surface

In the following section, we investigate the reaction of GL with an OH radical, which represents a key step in the aging process of NaCl. The potential energy surfaces of all possible pathways are presented in Figure 5, along with the optimized geometries of key stationary points. Starting from the most stable adsorption configuration of GL on NaCl (GL-NaCl-B1), the mixing of an OH radical with GL-NaCl-B1 was further explored to identify the initial states (IS) in the oxidation of GL. Several ISs were identified, and their optimized geometries are listed in Figure S4 along with the corresponding ΔE. As shown in IS1 of Figure 5, the O atom of the OH radical (O_{OH}) interacts with the Na atom of the NaCl surface, forming two O_{OH}–Na bonds with bond lengths of 2.36 and 2.40 Å. The energy for the formation of IS1 is −33.70 kcal mol^{-1}, indicating a strong interaction between the OH radical and the NaCl surface.

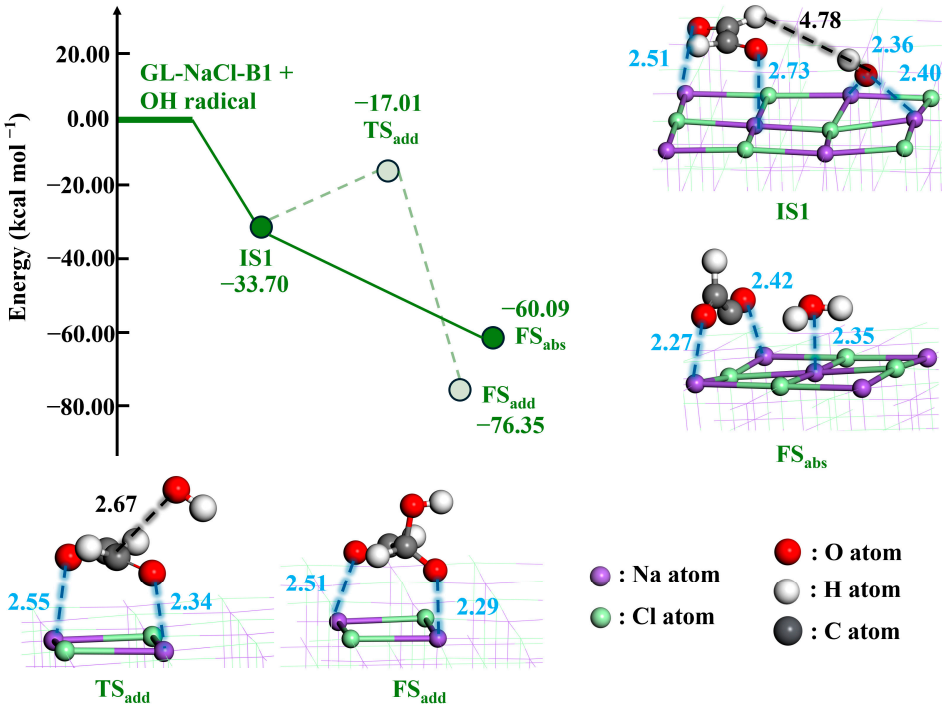

Figure 5. The potential energy surfaces of reaction pathways of GL and the OH radical along with the optimized geometries of key stationary points (bond lengths in Å).

Subsequently, the reaction of GL with the OH radical proceeds via two pathways, that is, the H-abstraction (R_{abs}) and OH-addition (R_{add}) pathways. For the H-abstraction pathway, the OH radical approaches the H atom of GL (H_{GL}), and H_{GL} is subsequently abstracted by the OH radical accompanied by the breaking of the C–H_{GL} bond. This process is barrierless. For the OH-addition pathway, the addition of the OH radical to the C atom of GL (C_{GL}) forms a C_{GL}–O_{OH} bond. However, the OH-addition pathway proceeds via a TS, with an energy barrier of 16.69 kcal mol^{-1}. This is because the OH radical must overcome its interaction with the NaCl surface and break two O_{OH}–Na bonds in IS1. Hence, R_{abs} is the dominant pathway for the reaction between GL and the OH radical, and the HC(O)CO radical is predicted to be the dominant product. To evaluate the possible influence of entropic effects, Gibbs free energy corrections were performed for the key stationary points at 298.15 K. Gibbs free energy profiles for the reaction pathway of GL and the OH radical are shown in Figure S5. The free energy barrier of R_{add} is 15.19 kcal mol^{-1}, whereas R_{abs} remains barrierless. Therefore, R_{abs} is the dominant pathway after considering entropic effects.

According to the previous study [40], the HC(O)CO radical is more reactive toward the reaction with methylamine and ammonia than GL. This radical reacts with methylamine/ammonia to form aminoalcohol radical intermediates, which are rapidly oxidized by O_2 to produce imine and diimine derivatives. These derivatives are important precursors of brown carbon. The barrierless formation of the HC(O)CO radical from the reaction of GL on NaCl implies that GL-driven aging processes are expected to significantly alter the optical properties of NaCl. In addition, the previous experimental studies also support the atmospheric uptake and reaction of GL on NaCl. Corrigan et al. [62] observed the RH-dependent uptake of GL by NaCl aerosol, suggesting that NaCl aerosol can serve as a reactive interface for GL. Shapiro et al. [63] observed high-molecular-weight secondary organic products in the mixing of GL and aqueous NaCl. Therefore, GL-driven aging represents an important atmospheric evolution process of sea salt particles. In the present study, the DFT calculations were performed using a single GL molecule on the NaCl surface to identify the interaction mechanism between GL and NaCl. Therefore, the effects of high GL coverage, as represented in MD simulations, were not considered in the DFT calculations. Under high coverage conditions, the adsorption mode of GL on NaCl can be influenced by intermolecular interactions among GL molecules, steric effects, and the competition for surface active sites. Hence, the influences of high GL coverage on the mixing between GL and NaCl remain a limitation of this study and should be further considered in future work. However, the dominant O_{GL}–Na interaction identified by DFT is consistent with the ADP and RDF results from MD simulations, indicating that the DFT calculations have captured the key interaction between GL and NaCl.

4. Conclusions and Atmospheric Implications

Atmospheric sea spray aerosol (SSA), one of the most abundant natural aerosol types, undergoes chemical aging during long-distance transport, leading to modifications of its chemical composition and physicochemical properties. However, the molecular-level aging mechanisms of SSA driven by OVOCs remain poorly understood. In this work, we investigated the aging processes of NaCl particles driven by GL, a representative OVOC, by using MD simulations and DFT calculations. MD simulation results reveal that GL can effectively mix with NaCl, with its carbonyl groups pointing toward the surface. DFT calculations identify the dominant interaction between O atoms of GL and Na atoms of NaCl surface, mediated by the formation of O_{GL}–Na bonds. Charge density difference analysis shows the electron transfer from surface Na atoms to the O atoms of GL, confirming the formation of strong interfacial interactions. The strength of the interaction between GL and NaCl is regulated by two key factors: the number of aldehyde groups involved in the interaction and the lengths of O_{GL}–Na bonds. Subsequently, the heterogeneous oxidation of GL by the OH radical proceeds via two competing pathways: the H-abstraction and OH addition pathways. The H-abstraction pathway is barrierless, whereas the OH-addition pathway requires an energy barrier of 16.69 kcal mol^{-1}. Thus, the H-abstraction pathway is the dominant pathway for the reaction of GL and the OH radical, forming the HC(O)CO radical. The HC(O)CO radical is highly reactive and can further undergo hydration and reaction with methylamine and ammonia to form light-absorbing compounds, thereby altering the radiative effects of SSA. Our results highlight the importance of considering GL-driven aging processes when investigating the physicochemical properties and atmospheric implications of sea salt particles. The present simulations were performed under dry conditions. In the atmosphere, variable relative humidity may influence SSA surface water coverage, ion mobility, and interfacial reactivity. Surface water molecules may compete with GL for surface active sites, weaken O_{GL}–Na interactions, or promote GL hydration. In addition, water molecules may affect the stabilization of OH radicals and transition

states, thereby altering the contribution of the H-abstraction and OH-addition pathways to the reaction of GL and the OH radical. Therefore, future studies using hydrated NaCl surfaces or deliquesced sea salt models are needed to further evaluate the influence of relative humidity on GL-driven aging.

Supplementary Materials: The following supporting information can be downloaded at https://www.mdpi.com/article/10.3390/toxics14050415/s1: Figure S1. Selected snapshots for the MD trajectories of uptake process of GL onto NaCl surface; Figure S2. Optimized geometries for adsorption configurations of GL on NaCl (bond lengths in Å); Figure S3. Potential energy surfaces for mixing pathways of GL with NaCl; Figure S4. Potential energy surfaces for the formation of ISs along with the corresponding optimized geometries (bond lengths in Å); Figure S5. Gibbs free energy profiles for reaction pathways of GL and OH radical.

Author Contributions: Conceptualization, Y.J. (Yuemeng Ji) and Y.J. (Yongpeng Ji); methodology, Y.J. (Yongpeng Ji) and Q.S.; validation, Q.S., J.W., and B.Z.; formal analysis and investigation, Y.J. (Yongpeng Ji), Z.Z., and S.C.; writing—original draft preparation, Y.J. (Yongpeng Ji); writing—review and editing, J.W., Y.J. (Yuemeng Ji), B.Z., W.Z., and J.C.; visualization, Y.J. (Yongpeng Ji), Z.Z. and S.C.; supervision and funding acquisition, Y.J. (Yuemeng Ji). All authors have read and agreed to the published version of the manuscript.

Funding: This work was financially supported by the National Natural Science Foundation of China (grant nos. 42577431, U25A20825, and 42077189), the Guangdong Basic and Applied Basic Research Foundation (grant no. 2025A1515011379) and the Technology Elite Navigation Project of Guangzhou (grant no. 2025A04J7038).

Institutional Review Board Statement: Not applicable.

Informed Consent Statement: Not applicable.

Data Availability Statement: The raw data supporting the conclusions of this article will be made available by the authors on request.

Conflicts of Interest: The authors declare no conflicts of interest.

References

1. Su, B.; Wang, T.; Zhang, G.; Liang, Y.; Lv, C.; Hu, Y.; Li, L.; Zhou, Z.; Wang, X.; Bi, X. A review of atmospheric aging of sea spray aerosols: Potential factors affecting chloride depletion. *Atmos. Environ.* **2022**, *290*, 119365. [CrossRef]
2. Quinn, P.K.; Collins, D.B.; Grassian, V.H.; Prather, K.A.; Bates, T.S. Chemistry and related properties of freshly emitted sea spray aerosol. *Chem. Rev.* **2015**, *115*, 4383–4399. [CrossRef]
3. Textor, C.; Schulz, M.; Guibert, S.; Kinne, S.; Balkanski, Y.; Bauer, S.; Berntsen, T.; Berglen, T.; Boucher, O.; Chin, M.; et al. Analysis and quantification of the diversities of aerosol life cycles within AeroCom. *Atmos. Chem. Phys.* **2006**, *6*, 1777–1813. [CrossRef]
4. Chi, J.W.; Li, W.J.; Zhang, D.Z.; Zhang, J.C.; Lin, Y.T.; Shen, X.J.; Sun, J.Y.; Chen, J.M.; Zhang, X.Y.; Zhang, Y.M.; et al. Sea salt aerosols as a reactive surface for inorganic and organic acidic gases in the Arctic troposphere. *Atmos. Chem. Phys.* **2015**, *15*, 11341–11353. [CrossRef]
5. Guo, J.; Luo, Y.; Yang, J.; Furtado, K.; Lei, H. Effects of anthropogenic and sea salt aerosols on a heavy rainfall event during the early-summer rainy season over coastal Southern China. *Atmos. Res.* **2022**, *265*, 105923. [CrossRef]
6. Lohmann, U.; Feichter, J. Global indirect aerosol effects: A review. *Atmos. Chem. Phys.* **2005**, *5*, 715–737. [CrossRef]
7. Burrows, S.M.; Hoose, C.; Pöschl, U.; Lawrence, M.G. Ice nuclei in marine air: Biogenic particles or dust? *Atmos. Chem. Phys.* **2013**, *13*, 245–267. [CrossRef]
8. Bondy, A.L.; Wang, B.; Laskin, A.; Craig, R.L.; Nhliziyo, M.V.; Bertman, S.B.; Pratt, K.A.; Shepson, P.B.; Ault, A.P. Inland Sea Spray Aerosol Transport and Incomplete Chloride Depletion: Varying Degrees of Reactive Processing Observed during SOAS. *Environ. Sci. Technol.* **2017**, *51*, 9533–9542. [CrossRef]
9. Rosati, B.; Christiansen, S.; Dinesen, A.; Roldin, P.; Massling, A.; Nilsson, E.D.; Bilde, M. The impact of atmospheric oxidation on hygroscopicity and cloud droplet activation of inorganic sea spray aerosol. *Sci. Rep.* **2021**, *11*, 10008. [CrossRef]
10. Carrico, C.M.; Kus, P.; Rood, M.J.; Quinn, P.K.; Bates, T.S. Mixtures of pollution, dust, sea salt, and volcanic aerosol during ACE-Asia: Radiative properties as a function of relative humidity. *J. Geophys. Res. Atmos.* **2003**, *108*, 8650. [CrossRef]

11. Randles, C.A.; Russell, L.M.; Ramaswamy, V. Hygroscopic and optical properties of organic sea salt aerosol and consequences for climate forcing. *Geophys. Res. Lett.* **2004**, *31*, L16108. [CrossRef]
12. Bougiatioti, A.; Nenes, A.; Fountoukis, C.; Kalivitis, N.; Pandis, S.N.; Mihalopoulos, N. Size-resolved CCN distributions and activation kinetics of aged continental and marine aerosol. *Atmos. Chem. Phys.* **2011**, *11*, 8791–8808. [CrossRef]
13. AzadiAghdam, M.; Braun, R.A.; Edwards, E.-L.; Bañaga, P.A.; Cruz, M.T.; Betito, G.; Cambaliza, M.O.; Dadashazar, H.; Lorenzo, G.R.; Ma, L.; et al. On the nature of sea salt aerosol at a coastal megacity: Insights from Manila, Philippines in Southeast Asia. *Atmos. Environ.* **2019**, *216*, 116922. [CrossRef]
14. Bertram, T.H.; Cochran, R.E.; Grassian, V.H.; Stone, E.A. Sea spray aerosol chemical composition: Elemental and molecular mimics for laboratory studies of heterogeneous and multiphase reactions. *Chem. Soc. Rev.* **2018**, *47*, 2374–2400. [CrossRef]
15. Ghorai, S.; Wang, B.; Tivanski, A.; Laskin, A. Hygroscopic properties of internally mixed particles composed of NaCl and water-soluble organic acids. *Environ. Sci. Technol.* **2014**, *48*, 2234–2241. [CrossRef]
16. Li, W.; Sun, J.; Xu, L.; Shi, Z.; Riemer, N.; Sun, Y.; Fu, P.; Zhang, J.; Lin, Y.; Wang, X.; et al. A conceptual framework for mixing structures in individual aerosol particles. *J. Geophys. Res. Atmos.* **2016**, *121*, 13784–13798. [CrossRef]
17. Woods, E.; Chung, D.; Lanney, H.M.; Ashwell, B.A. Surface Morphology and Phase Transitions in Mixed NaCl/$MgSO_4$ Aerosol Particles. *J. Phys. Chem. A* **2010**, *114*, 2837–2844. [CrossRef] [PubMed]
18. Laskin, A.; Moffet, R.C.; Gilles, M.K.; Fast, J.D.; Zaveri, R.A.; Wang, B.; Nigge, P.; Shutthanandan, J. Tropospheric chemistry of internally mixed sea salt and organic particles: Surprising reactivity of NaCl with weak organic acids. *J. Geophys. Res. Atmos.* **2012**, *117*, D15302. [CrossRef]
19. Wang, S.; Yuan, B.; Wu, C.; Wang, C.; Li, T.; He, X.; Huangfu, Y.; Qi, J.; Li, X.-B.; Sha, Q.e.; et al. Oxygenated volatile organic compounds (VOCs) as significant but varied contributors to VOC emissions from vehicles. *Atmos. Chem. Phys.* **2022**, *22*, 9703–9720. [CrossRef]
20. Karl, T.; Guenther, A.; Spirig, C.; Hansel, A.; Fall, R. Seasonal variation of biogenic VOC emissions above a mixed hardwood forest in northern Michigan. *Geophys. Res. Lett.* **2003**, *30*, 2186. [CrossRef]
21. Mellouki, A.; Wallington, T.J.; Chen, J. Atmospheric Chemistry of Oxygenated Volatile Organic Compounds: Impacts on Air Quality and Climate. *Chem. Rev.* **2015**, *115*, 3984–4014. [CrossRef]
22. Gentner, D.R.; Worton, D.R.; Isaacman, G.; Davis, L.C.; Dallmann, T.R.; Wood, E.C.; Herndon, S.C.; Goldstein, A.H.; Harley, R.A. Chemical Composition of Gas-Phase Organic Carbon Emissions from Motor Vehicles and Implications for Ozone Production. *Environ. Sci. Technol.* **2013**, *47*, 11837–11848. [CrossRef] [PubMed]
23. Carter, W.P.L. Development of ozone reactivity scales for volatile organic compounds. *Air Waste* **1994**, *44*, 881–899. [CrossRef]
24. Roberts, J.M.; Stroud, C.A.; Jobson, B.T.; Trainer, M.; Hereid, D.; Williams, E.; Fehsenfeld, F.; Brune, W.; Martinez, M.; Harder, H. Application of a sequential reaction model to PANs and aldehyde measurements in two urban areas. *Geophys. Res. Lett.* **2001**, *28*, 4583–4586. [CrossRef]
25. Clifford, G.M.; Hadj-Aissa, A.; Healy, R.M.; Mellouki, A.; Munoz, A.; Wirtz, K.; Martin Reviejo, M.; Borras, E.; Wenger, J.C. The atmospheric photolysis of o-tolualdehyde. *Environ. Sci. Technol.* **2011**, *45*, 9649–9657. [CrossRef]
26. Ji, Y.; Zheng, J.; Qin, D.; Li, Y.; Gao, Y.; Yao, M.; Chen, X.; Li, G.; An, T.; Zhang, R. OH-Initiated Oxidation of Acetylacetone: Implications for Ozone and Secondary Organic Aerosol Formation. *Environ. Sci. Technol.* **2018**, *52*, 11169–11177. [CrossRef]
27. Mang, S.A.; Henricksen, D.K.; Bateman, A.P.; Andersen, M.P.S.; Blake, D.R.; Nizkorodov, S.A. Contribution of carbonyl photochemistry to aging of atmospheric secondary organic aerosol. *J. Phys. Chem. A* **2008**, *112*, 8337–8344. [CrossRef]
28. Fu, T.-M.; Jacob, D.J.; Wittrock, F.; Burrows, J.P.; Vrekoussis, M.; Henze, D.K. Global budgets of atmospheric glyoxal and methylglyoxal, and implications for formation of secondary organic aerosols. *J. Geophys. Res. Atmos.* **2008**, *113*, D15303. [CrossRef]
29. Myriokefalitakis, S.; Vrekoussis, M.; Tsigaridis, K.; Wittrock, F.; Richter, A.; Brühl, C.; Volkamer, R.; Burrows, J.P.; Kanakidou, M. The influence of natural and anthropogenic secondary sources on the glyoxal global distribution. *Atmos. Chem. Phys.* **2008**, *8*, 4965–4981. [CrossRef]
30. Ling, Z.; Xie, Q.; Shao, M.; Wang, Z.; Wang, T.; Guo, H.; Wang, X. Formation and sink of glyoxal and methylglyoxal in a polluted subtropical environment: Observation-based photochemical analysis and impact evaluation. *Atmos. Chem. Phys.* **2020**, *20*, 11451–11467. [CrossRef]
31. Volkamer, R.; Martini, F.S.; Molina, L.T.; Salcedo, D.; Jimenez, J.L.; Molina, M.J. A missing sink for gas-phase glyoxal in Mexico City: Formation of secondary organic aerosol. *Geophys. Res. Lett.* **2007**, *34*, L19807. [CrossRef]
32. Wennberg, P.O.; Bates, K.H.; Crounse, J.D.; Dodson, L.G.; McVay, R.C.; Mertens, L.A.; Nguyen, T.B.; Praske, E.; Schwantes, R.H.; Smarte, M.D.; et al. Gas-Phase Reactions of Isoprene and Its Major Oxidation Products. *Chem. Rev.* **2018**, *118*, 3337–3390. [CrossRef]
33. Lin, X.; Huang, M.; Zhu, M.; Zhao, W.; Gu, X.; Zhang, W. Theoretical study on atmospheric gaseous reactions of glyoxal with sulfuric acid and ammonia. *Comput. Theor. Chem.* **2023**, *1219*, 113950. [CrossRef]
34. Gomez, M.E.; Lin, Y.; Guo, S.; Zhang, R. Heterogeneous Chemistry of Glyoxal on Acidic Solutions. An Oligomerization Pathway for Secondary Organic Aerosol Formation. *J. Phys. Chem. A* **2015**, *119*, 4457–4463. [CrossRef]

35. Ji, Y.; Shi, Q.; Ma, X.; Gao, L.; Wang, J.; Li, Y.; Gao, Y.; Li, G.; Zhang, R.; An, T. Elucidating the critical oligomeric steps in secondary organic aerosol and brown carbon formation. *Atmos. Chem. Phys.* **2022**, *22*, 7259–7271. [CrossRef]
36. Avzianova, E.; Brooks, S.D. Raman spectroscopy of glyoxal oligomers in aqueous solutions. *Spectrochim. Acta Part A* **2013**, *101*, 40–48. [CrossRef] [PubMed]
37. De Haan, D.O.; Jansen, K.; Rynaski, A.D.; Sueme, W.R.P.; Torkelson, A.K.; Czer, E.T.; Kim, A.K.; Rafla, M.A.; De Haan, A.C.; Tolbert, M.A. Brown Carbon Production by Aqueous-Phase Interactions of Glyoxal and SO_2. *Environ. Sci. Technol.* **2020**, *54*, 4781–4789. [CrossRef] [PubMed]
38. Michailoudi, G.; Lin, J.J.; Yuzawa, H.; Nagasaka, M.; Huttula, M.; Kosugi, N.; Kurtén, T.; Patanen, M.; Prisle, N.L. Aqueous-phase behavior of glyoxal and methylglyoxal observed with carbon and oxygen K-edge X-ray absorption spectroscopy. *Atmos. Chem. Phys.* **2021**, *21*, 2881–2894. [CrossRef]
39. Shen, X.; Wu, H.; Zhao, Y.; Huang, D.; Huang, L.; Chen, Z. Heterogeneous reactions of glyoxal on mineral particles: A new avenue for oligomers and organosulfate formation. *Atmos. Environ.* **2016**, *131*, 133–140. [CrossRef]
40. Guo, Z.; Zhang, W.; Zhao, B.; Gao, L.; Ji, Y.; Ji, Y. Photooxidation browning mechanism of small α-dicarbonyl compounds on natural mineral particle in the presence of methylamine/ammonia. *Chem. Phys. Lett.* **2023**, *810*, 140187. [CrossRef]
41. Shi, Q.; Zhang, W.; Ji, Y.; Wang, J.; Qin, D.; Chen, J.; Gao, Y.; Li, G.; An, T. Enhanced uptake of glyoxal at the acidic nanoparticle interface: Implications for secondary organic aerosol formation. *Environ. Sci. Nano* **2020**, *7*, 1126–1135. [CrossRef]
42. Mabato, B.R.G.; Gen, M.; Chu, Y.; Chan, C.K. Reactive Uptake of Glyoxal by Methylaminium-Containing Salts as a Function of Relative Humidity. *ACS Earth Space Chem.* **2019**, *3*, 150–157. [CrossRef]
43. Qin, Y.; Ye, J.; Ohno, P.E.; Lei, Y.; Wang, J.; Liu, P.; Thomson, R.J.; Martin, S.T. Synergistic Uptake by Acidic Sulfate Particles of Gaseous Mixtures of Glyoxal and Pinanediol. *Environ. Sci. Technol.* **2020**, *54*, 11762–11770. [CrossRef]
44. De Haan, D.O.; Hawkins, L.N.; Jansen, K.; Welsh, H.G.; Pednekar, R.; de Loera, A.; Jimenez, N.G.; Tolbert, M.A.; Cazaunau, M.; Gratien, A.; et al. Glyoxal's impact on dry ammonium salts: Fast and reversible surface aerosol browning. *Atmos. Chem. Phys.* **2020**, *20*, 9581–9590. [CrossRef]
45. Battaglia, F.; Formenti, P.; Giorio, C.; Cazaunau, M.; Pangui, E.; Bergé, A.; Gratien, A.; Pereira, D.L.; Bertin, T.; de Brito, J.F.; et al. Formation and composition of organic aerosols from the uptake of glyoxal on natural mineral dust aerosols: A laboratory study. *Atmos. Chem. Phys.* **2025**, *25*, 12409–12431. [CrossRef]
46. Thompson, A.P.; Aktulga, H.M.; Berger, R.; Bolintineanu, D.S.; Brown, W.M.; Crozier, P.S.; in 't Veld, P.J.; Kohlmeyer, A.; Moore, S.G.; Nguyen, T.D.; et al. LAMMPS—A flexible simulation tool for particle-based materials modeling at the atomic, meso, and continuum scales. *Comput. Phys. Commun.* **2022**, *271*, 108171. [CrossRef]
47. Jing, X.; Chen, Z.; Cao, X.; Huang, Q.; Liu, P.; Zhang, Y.-h. Rapid Sulfate Formation via Mn2+-Catalyzed SO2 Oxidation on the Surface of NaCl Microdroplets. *J. Phys. Chem. C* **2023**, *127*, 13632–13638. [CrossRef]
48. Kruse, S.M.; Slade, J.H. Heterogeneous and Photosensitized Oxidative Degradation Kinetics of the Plastic Additive Bisphenol-A in Sea Spray Aerosol Mimics. *J. Phys. Chem. A* **2023**, *127*, 4724–4733. [CrossRef]
49. Shinoda, W.; Shiga, M.; Mikami, M. Rapid estimation of elastic constants by molecular dynamics simulation under constant stress. *Phys. Rev. B* **2004**, *69*, 134103. [CrossRef]
50. Tuckerman, M.E.; Alejandre, J.; López-Rendón, R.; Jochim, A.L.; Martyna, G.J. A Liouville-operator derived measure-preserving integrator for molecular dynamics simulations in the isothermal–isobaric ensemble. *J. Phys. A Math. Gen.* **2006**, *39*, 5629–5651. [CrossRef]
51. Joung, I.S.; Cheatham, T.E., III. Determination of Alkali and Halide Monovalent Ion Parameters for Use in Explicitly Solvated Biomolecular Simulations. *J. Phys. Chem. B* **2008**, *112*, 9020–9041. [CrossRef]
52. Wang, J.; Wolf, R.M.; Caldwell, J.W.; Kollman, P.A.; Case, D.A. Development and testing of a general amber force field. *J. Comput. Chem.* **2004**, *25*, 1157–1174. [CrossRef] [PubMed]
53. Plimpton, S.; Pollock, R.; Stevens, M.J. Particle Mesh Ewald and RRESPA for Parallel Molecular Dynamics Simulations. In *Proceedings of The Eighth SIAM Conference on Parallel Processing for Scientific Computing, Minneapolis, MN, USA, 14–17 March 1997*; Society for Industrial and Applied Mathematics: Philadelphia, PA, USA, 1997; pp. 1–13.
54. Kresse, G.; Furthmüller, J. Efficient iterative schemes for ab initio total-energy calculations using a plane-wave basis set. *Phys. Rev. B* **1996**, *54*, 11169–11186. [CrossRef]
55. Perdew, J.P.; Chevary, J.A.; Vosko, S.H.; Jackson, K.A.; Pederson, M.R.; Singh, D.J.; Fiolhais, C. Atoms, molecules, solids, and surfaces: Applications of the generalized gradient approximation for exchange and correlation. *Phys. Rev. B* **1993**, *46*, 6671. [CrossRef] [PubMed]
56. Blöchl, P.E. Projector augmented-wave method. *Phys. Rev. B* **1994**, *50*, 17953. [CrossRef]
57. Grimme, S.; Antony, J.; Ehrlich, S.; Krieg, H. A consistent and accurate ab initio parametrization of density functional dispersion correction (DFT-D) for the 94 elements H-Pu. *J. Chem. Phys.* **2010**, *132*, 154104. [CrossRef] [PubMed]
58. Grimme, S.; Ehrlich, S.; Goerigk, L. Effect of the Damping Function in Dispersion Corrected Density Functional Theory. *J. Comput. Chem.* **2011**, *32*, 1456–1465. [CrossRef]

59. Henkelman, G.; Uberuaga, B.P.; Jonsson, H. A climbing image nudged elastic band method for finding saddle points and minimum energy paths. *J. Chem. Phys.* **2000**, *113*, 9901–9904. [CrossRef]
60. Heyden, A.; Bell, A.T.; Keil, F.J. Efficient methods for finding transition states in chemical reactions: Comparison of improved dimer method and partitioned rational function optimization method. *J. Chem. Phys.* **2005**, *123*, 224101. [CrossRef]
61. Momma, K.; Izumi, F. VESTA 3 for three-dimensional visualization of crystal, volumetric and morphology data. *J. Appl. Crystallogr.* **2011**, *44*, 1272–1276. [CrossRef]
62. Corrigan, A.L.; Hanley, S.W.; De Haan, D.O. Uptake of Glyoxal by Organic and Inorganic Aerosol. *Environ. Sci. Technol.* **2008**, *42*, 4428–4433. [CrossRef] [PubMed]
63. Shapiro, E.L.; Szprengiel, J.; Sareen, N.; Jen, C.N.; Giordano, M.R.; McNeill, V.F. Light-absorbing secondary organic material formed by glyoxal in aqueous aerosol mimics. *Atmos. Chem. Phys.* **2009**, *9*, 2289–2300. [CrossRef]